ChemCatChem

Research Article
doi.org/10.1002/cctc.202500789

Chemistry Europe
European Chemical Societies Publishing

www.chemcatchem.org

Efficient Mesoporous $NiCeLaO_x$-Based Catalysts Prepared by Nanocasting for the RWGS Reaction

Belén Bachiller-Baeza,*[a] Jiajie Wu,[a] Mónica García-García,[a] José Antonio Alonso,[b] and Consuelo Alvarez-Galván*[a]

In this work, the influence of the porous structure of the catalyst, as well as the effect of La doping on the performance of Ni-ceria-based catalysts for the reverse water-gas shift reaction (rWGS) has been studied. Thus, Ni-ceria and Ni-La doped ceria catalysts have been prepared using nanocasting or hard-templating method, also studying the influence of the incorporation method of the nickel phase. Samples prepared by sol-gel were also prepared for comparison. The catalysts were tested in the rWGS and characterized by different techniques: X-ray diffraction (XRD), electron microscopy (TEM and STEM-EDX), adsorption-desorption N_2 isotherms (BET), temperature programmed reduction (TPR-H_2), and X-ray photoelectron spectroscopy. The results obtained indicate that the mesoporous catalysts prepared by hard-templating, regardless of the nickel incorporation method have developed a mesoporous structure and a relatively large specific surface area that increases CO formation per catalyst weight, compared to those prepared by sol-gel. The method of incorporating Ni into mesoporous catalysts influences the level of catalyst deactivation and the evolution of CO selectivity with reaction time.

1. Introduction

The conversion of CO_2 into CO by catalytic reduction with H_2 (reverse water-gas shift reaction, rWGS, $CO_2 + H_2 \rightleftarrows CO + H_2O$) is considered one of the most promising processes for the valorization and utilization of CO_2, constituting a first stage for the production of fuels and chemical products.[1,2] The second stage would be the use of synthesis gas (syngas) in the production of hydrocarbons and/or oxygenated hydrocarbons through the Fischer-Tropsch process or in the synthesis of methanol for the subsequent production of fuels or synthetic polymers, among other products.

Typical catalysts for the rWGS reaction consist of well-isolated and dispersed metal nanoparticles (NPs), usually supported on a reducible oxide, to maximize the interface between the metal and the support, since both phases are involved in the rWGS chemistry.[3,4] This is related to a probable bifunctional mechanism, where the metal particles activate the dissociation of H_2 and the oxygen vacancies existing in the reducible oxide network favour the adsorption and dissociation of CO_2, promoting the formation of CO and H_2O due to the proximity between both phases in the interface. Thus, the reaction of H atoms existing in the metal particles and oxygen from the support network to form H_2O is favoured when the interface is large. Among the metals studied in literature, from noble to transition metals,[5–7] nickel is considered a good candidate for reactions involving CO_2 due to its low price and relative stability. Concerning the reducible metal oxide, cerium oxide has been revealed as an excellent choice due to its unique chemical properties, as the creation of surface oxygen vacancies when reduced.[8]

However, Ni-based catalysts for RWGS reaction tend to form CH_4 as by-product which decreases the efficiency of the subsequent use of the syngas since an additional separation step would be required. In addition, it has been observed that nickel-based catalysts suffer some deactivation during the reaction, due to the relatively large size of the Ni NPs and their possible sintering, which would favour the generation of carbon deposits.[9] Moreover, this kind of ceria-supported catalysts are characterized by very low surface area values and an increase in this parameter is expected to considerably improve the catalytic performance of these materials. Therefore, the development of a new catalytic system with excellent activity and stability under working conditions is important for further exploiting RWGS, yet is still a big challenge.

This deactivation could be suppressed to a certain extent by depositing the nanoparticles of the active metal on oxide materials with a large specific surface area and a structure rich in pores to improve the dispersion of the metal, which together with a possible "confinement effect" in the pores could effectively control the agglomeration of Ni particles as well as the metal-support interaction. In this sense, very promising results in the rWGS reaction have been obtained on catalysts prepared by

[a] B. Bachiller-Baeza, J. Wu, M. García-García, C. Alvarez-Galván
Instituto de Catálisis y Petroleoquímica, CSIC, Cantoblanco, Madrid 28049, Spain
E-mail: b.bachiller@icp.csic.es
c.alvarez@icp.csic.es

[b] J. A. Alonso
Instituto de Ciencia de Materiales de Madrid, CSIC, Cantoblanco, Madrid 28049, Spain

Supporting information for this article is available on the WWW under https://doi.org/10.1002/cctc.202500789

solution combustion synthesis (SCS) with random, but not easily controllable, macroporosity.[10]

On the other hand, the incorporation of lanthanides as dopants in CeO_2 seems to improve the catalytic performance and stability, creating oxygen vacancies and modulating the release of oxygen from the support. Thus, it has been found that catalysts with low Ni content and with CeO_2 type supports doped with lanthanum show excellent catalytic activity and stability during the rWGS reaction. In addition, the presence of La modifies the surface acid-base properties of the support forming a phase of surface lanthanum oxycarbonate, which has a role in the gasification of carbonaceous precursors.[11]

Ordered mesoporous metal oxides have gained researching interest due to their high surface areas and larger pore size distributions.[12,13] In general, the synthesis method of these materials has a pronounced impact on their properties and consequently on the catalytic activity.[14,15] In the case of ceria, in addition, a mesoporous nanostructure with a large surface area to volume ratio would have more catalytic active centres on the surface and oxygen storage capacity (OSC) than a bulk ceria, being then more effective for catalytic applications.[16] Among the methods used for the synthesis of mesoporous metal oxides, the nanocasting or hard-templating method applying mesoporous silicas (such as SBA-15, KIT-6, and SBA-16) as templates is an attractive and promising alternative. SBA-15 has high specific surface area, thermal stability, and presents uniform cylindrical mesopores of adjustable size that are interconnected by micropores, allowing mass diffusion within the ordered structure. These properties have promoted interest in its use as a catalysts support and as a template to produce mesoporous metal oxides for different applications.[17–20]

Taking this into account, the main objective of this work has been to prepare Ni-ceria catalysts with controlled mesoporous structures using the hard-templating method, trying to optimize the pore geometry and pore size. The high porosity of these catalysts, apart from increasing the dispersion and modifying the interaction of the metal nanoparticles with the support, could reduce the pressure drop, heat and mass transfer, and the formation of hot spots during the reaction, which would decreasealso the probability of sintering and carbon formation. Furthermore, we have synthesized our materials using two preparation methods for the incorporation of Ni: in situ doping or one-pot, adding all the cations at the same time, and wet impregnation on the synthesized ceria-based oxide. Therefore, the purpose of this research was to evaluate the effect of preparation method on the structure, surface chemistry and activity in the reverse water-gas shift reaction for the mesoporous Ni/CeO_2 catalysts.

2. Experimental Section

2.1. Preparation of Supports and Catalysts

Mesoporous catalysts were prepared by the hard-templating method, in which the mesoporous silica that was studied as a template was SBA-15. The SBA-15 was prepared according to what is reported in the literature.[21,22] Briefly, the Pluronic P123 polymer (7.2 g) was dissolved in water (234 g) and concentrated HCl (34 g) at room temperature and left stirring until the polymer was completely dissolved. Subsequently, TEOS (15 g) was added and stirred for 24 h at 308 K. Afterwards, a hydrothermal treatment was carried out at 373 K for 24 h. The suspension was then filtered and dried at 373 K for 12 h. Finally, the white solid was washed with water and ethanol and calcined at 823 K for 5 h in static air (heating rate of 1.5 K/min).

For the synthesis of the Ni-based mesoporous oxides, two strategies were employed: direct preparation of mesoporous binary $NiO\text{-}CeO_2$ (and ternary $NiO\text{-}CeO_2\text{-}La_2O_3$) mixed oxides or preparation of supported mesoporous catalysts by impregnation of Ni on previously prepared mesoporous ceria (and La doped-ceria) supports.

Then, for the synthesis of the mesoporous binary (and ternary) mixed oxides catalysts, NiCe-mix (and NiCeLa-mix), first, the corresponding stoichiometric amounts of $Ni(NO_3)_2{\cdot}6H_2O$ and $Ce(NO_3)_3{\cdot}6H_2O$ (or $Ni(NO_3)_2{\cdot}6H_2O$, $Ce(NO_3)_3{\cdot}6H_2O$ and $La(NO_3)_3{\cdot}6H_2O$), to achieve 10 mol% Ni (and 10 mol% La) were mixed together in a single pot in ethanol (25 mL). The mesoporous silica SBA-15 (Ce/Si atomic ratio = 1.4) was added and the dispersion was kept under constant stirring until the ethanol evaporated. Afterwards, the catalyst was dried at 323 K overnight and subsequently calcined at 573 K for 2 h (ramp 3 h and 20 min). After this calcination, in order to achieve a higher loading, the impregnation step was repeated a second time under the same conditions. After drying at 323 K, the samples were finally calcined at 773 K for 5 h. The removal of the silica template was performed by chemical etching with a 2 M NaOH aqueous solution at 333 K for 12 h, followed by filtering, washing with water and ethanol several times and drying at 373 K.

For the second strategy, i.e., impregnation on mesoporous supports, first pure cerium oxide and cerium oxide doped with La (10% molar) were synthetized following the same steps as in the previous protocol but with only $Ce(NO_3)_3{\cdot}6H_2O$ (and $La(NO_3)_3{\cdot}6H_2O$) precursors. The incorporation of Ni (10% molar) on the obtained mesoporous oxides was carried out by impregnating the supports (0.8 g) with a solution of $Ni(NO_3)_2{\cdot}6H_2O$ in ethanol-water (1:1). It was left stirring until the solvent was evaporated. The solids were dried at 323 K for 12 h and finally calcined at 773 K to obtain NiCe-imp and NiCeLa-imp catalysts.

For comparison, the samples NiCe-sg ($Ni_{0.1}/(CeO_2)_{0.9}$) and NiCeLa-sg ($Ni_{0.1}/(Ce_{0.9}La_{0.1}O_{1.95})_{0.9}$) were also prepared by a sol-gel method using trisodium citrate dihydrate ($Na_3C_6H_5O_7{\cdot}2H_2O$), as a metal ion chelating agent.[23] The corresponding stoichiometric amounts of the metal precursors ($Ni(NO_3)_2{\cdot}6H_2O$, $Ce(NO_3)_3{\cdot}6H_2O$, $La(NO_3)_3{\cdot}6H_2O$) are mixed with a volume of the citrate solution in water (0.34 M), but maintaining the sodium citrate/metal cations ratio = 1.1. The solution obtained is stirred and heated to 473 K on a hot plate. Once water is nearly totally evaporated, a green gel forms at the bottom of the glass which is subsequently calcined at 573 K for 2 h (0.5 K/min). Finally, the powder obtained is ground and calcined at 1073 K for 4 h (2 K/min).

2.2. Catalyst Characterization

The crystalline structure of the materials was determined by X-ray diffraction (PANalytical X´Pert Pro) using CuKα radiation (λ = 1.5406 Å). The wide diffraction patterns were measured with a 2θ scan between 2° and 90°, with a step of 0.02° and accumulation time of 50 s per point. Low-angle diffraction were collected in the range 2θ = 0.4°–6°, with an accumulation time of 20 s per point.

The morphology was analysed by taking scanning electron microscopy (SEM) images on a Hitachi TM-1000 equipment. For high resolution images a NanoSEM 230 (FEI) field emission scanning elec-

tron microscope (FE-SEM) was used. Analysis by energy dispersive X-ray spectroscopy (EDX) was performed to check the composition of the catalysts and the possible presence of residual silica template. Further characterization of the samples was performed by transmission and scanning transmission electron microscopy (TEM and STEM) and EDX by using a JEOL 3100 or a field emission gun (FEG) JEOL 2100F microscope operated at 200 kV. To prepare TEM samples, the specimens were treated by sonicating in absolute ethanol for several minutes, and a few drops of the resulting suspension were deposited onto a holey-carbon film supported on a copper grid, which was subsequently dried.

The BET surface area of the samples was estimated from the N_2 adsorption-desorption isotherms obtained at 77 K, taking a value of 0.162 nm^2 for the cross section of the N_2 molecule adsorbed at this temperature. These measurements were carried out with a Micromeritics ASAP 2000 apparatus on samples previously degassed at 393 K for 13 h.

X-ray fluorescence analysis (XRF; Bruker S2 PicoFox) of the powders was performed to estimate the bulk chemical composition of the prepared catalysts.

The temperature programmed reduction (TPR) experiments were carried out on a Micromeritics TPD/TPR 2900 equipment. After the pretreatment of the catalyst in helium at 383 K for 15 min, the reduction profile was recorded by heating the sample from room temperature to 1073 K with a ramp of 10 K/min under a flow of H_2/Ar (10% v/v).

The X-ray photoelectron spectra of the samples were recorded using a SPECS GmbH spectrometer equipped with a PHOIBOS 150 9MCD analyzer and a non-monochromatic Mg X-ray source with a pass energy of 50 eV. Each sample was pressed into a small pellet, placed in the sample holder and degassed in the chamber for 6–8 h to achieve a dynamic vacuum below 10^{-8} Pa before analysis. Catalysts were reduced in the pretreatment chamber (HPC) under a 15% H_2 in N_2 gas mixture at 873 K for 2 h. The spectral data were analysed using CASA XPS software.[24] The binding energy is referenced to the C 1s line at 284.6 eV.

2.3. Catalytic Activity Tests: rWGS

The reaction (rWGS) was carried out in a continuous flow fixed bed quartz tubular reactor (4 mm, inner diameter) under atmospheric pressure and a space velocity of 600,000 $mL_N \cdot h^{-1} \cdot g^{-1}$. The molar composition of the reaction mixture was 60% H_2, 30% CO_2, and 10% N_2. The reaction stream was analyzed online by gas chromatography (HP 6890), with a Carboxen 1010 PLOT column (SUPELCO) and a TCD detector. Nitrogen was used as an internal standard for quantification. The catalyst (sieve between 100 and 200 μm) was activated under the reactive feed up to 873 K and tested at the same temperature for approximately 24 h.

3. Results and Discussion

3.1. XRD Results

Low-angle diffractogram of the SBA-15 sample used as template (Figure 1) confirms the success of the synthesis and the 2D structural order with a symmetry corresponding to the hexagonal crystalline system and the 2D hexagonal P6mm space group.[21,25] On the other hand, mesoporous materials prepared using the synthesized SBA-15 as template present a peak close to 2θ = 1°, which correspond to the (211) plane and would confirm the ordered mesoporous structure of the materials.[18,26] The low intensity of the peaks compared to those of the hard template silica suggests less ordered materials as frequently found for this type of replicas.[19]

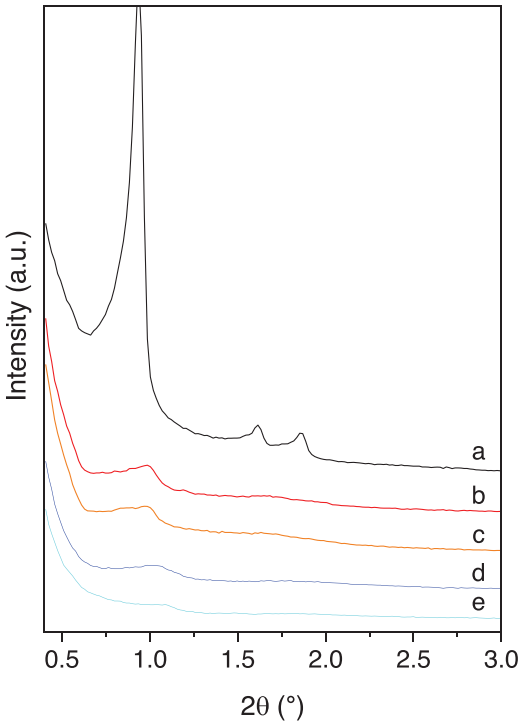

Figure 1. Low-angle XRD of a) SBA-15 and mesoporous supports, and catalysts prepared using the SBA-15 as template b) CeO_2-m, c) CeLa-m, d) NiCe-mix, and e) NiCeLa-mix.

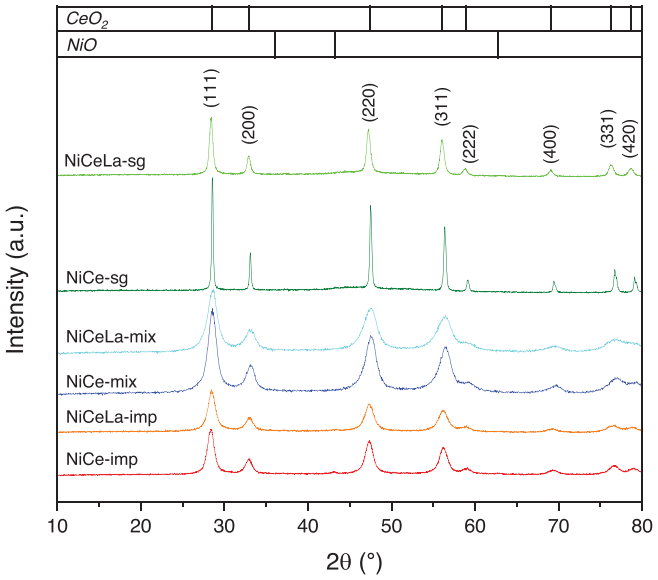

Figure 2. XRD patterns for all the prepared Ni catalysts.

Figure 2 shows the wide-angle diffractograms of all the synthesized catalysts. The diffractograms of the mesoporous supports CeO_2-m and CeLa-m are displayed in Figure S1. All of them show well-resolved peaks at 2θ = 28.5°, 33.1°, 47.6°, 56.4°, 59.2°, 69.5°, 76.7°, and 79.2°, characteristic of the fluorite-

Table 1. Average crystallite sizes and Unit-cell parameters determined by Rietveld refinement from XRD data. Space group *Fm-3m*. Discrepancy factors (χ^2 and R_{Bragg}) are also indicated.

Sample	Lattice parameter (Å)	χ^2	R_{Bragg} (%)	Average crystallite sizes (nm)[a)]
CeO_2	5.4180(8)	2.35	4.76	8.3
CeLa	5.4286(7)	1.91	1.82	8.3
NiCe-imp	5.4116(6)	2.77	1.99	8.7
NiCeLa-imp	5.4308(9)	5.46	2.52	8.0
NiCe-mix	5.405(1)	3.05	3.04	7.0
NiCeLa-mix	5.423(1)	3.77	2.46	6.0
NiCe-sg	5.4108(2)	9.4	5.44	58.6
NiCeLa-sg	5.4402(4)	12.1	3.83	19.9

[a)] Calculation from CeO_2 (111) in the XRD pattern using the Scherrer equation.

type structure (face-centered cubic, space group Fm-3m) of CeO_2 (JCPDS 43–1002). The more intense and narrower peaks obtained in the samples prepared by sol-gel indicate that these samples have greater crystallinity and that the crystalline domain has a larger size. Besides, the peak widths of the catalysts became broader with the incorporation of La, indicating a decrease of the average domain size The average domain size of the oxide crystallites obtained by calculation using the Scherrer formula (Table 1) corroborate these facts. According to XRD, the lack of diffraction at $2\theta \sim 22°$, typical of silica, and the low base line in the patterns—related to amorphous phases— indicates the almost complete removal of the template and a high degree of crystallinity.

For the samples prepared by impregnation (NiCe-imp and NiCeLa-imp), small peaks were observed at 37.4, 43.1, and 62.9°, corresponding to the {111}, {200}, and {220} planes of NiO (JCPDS 04–0835) which would confirm the presence of NiO as a crystallized phase on the surface of the mesoporous supports. The absence of these peaks for the NiCe-mix, NiCeLa-mix, NiCe-sg and NiCeLa-sg samples suggest that the Ni is incorporated on the CeO_2 phase or that the NiO average domain is too small to be observed by this technique. Small shifts in the XRD peaks for the La-doped samples seem to indicate that La is partially replacing some positions of Ce^{4+} within the CeO_2 crystal lattice.

Rietveld fits from laboratory XRD data were performed for the samples. Plots for two characteristic samples are shown in Figure S1. A single fluorite-type phase was identified in all cases; no traces of minor impurities or secondary phases were observed. The goodness of fit demonstrates the quality of the two samples. The refinement was performed in the *Fm-3m* space group, with Ce at positions 4*a* (0,0,0) and O at 8**c** (1/4,1/4,1/4). In the case of the samples with 10% La, this element was statistically distributed at the Ce positions. The isotropic thermal factors of all atoms, as well as the O occupancy factor, were refined. Table 1 shows the unit-cell parameters determined for all the samples. Notice the great precision with which the unit cell parameters are determined, up to the fourth significant figure. Some facts can be highlighted: i) the lattice parameter for pristine mesoporous CeO_2 fits well with those reported in literature, ranging 5.41–5.42 Å; ii) the incorporation of larger La^{3+} ions (1.16 Å) into the Ce^{4+} (0.97 Å in eightfold coordination) crystallographic sites implies an expansion of the unit cell, reaching 5.4402(4) Å for the sample NiCeLa-sg and 5.4308(9) for the sample NiCeLa-imp iii) the unit-cell contraction down to 5.405(1) Å for NiCe-mix suggests the incorporation of a certain proportion of Ni^{2+} ions into the Ce sublattice, the former being considerable smaller (0.83 Å for Ni^{2+} in octahedral coordination) than Ce^{4+} ions. For the NiCeLa-mix sample, the obtained value could be explained by a simultaneous incorporation of Ni^{2+} and La^{3+} where two opposite effects, i.e., shrinking (due to Ni incorporation) and expansion (due to La incorporation) can be compensated. The possibility that Ni^{2+} replaces Ce^{4+} in the fluorite oxide matrix has been demonstrated by DFT calculations, the

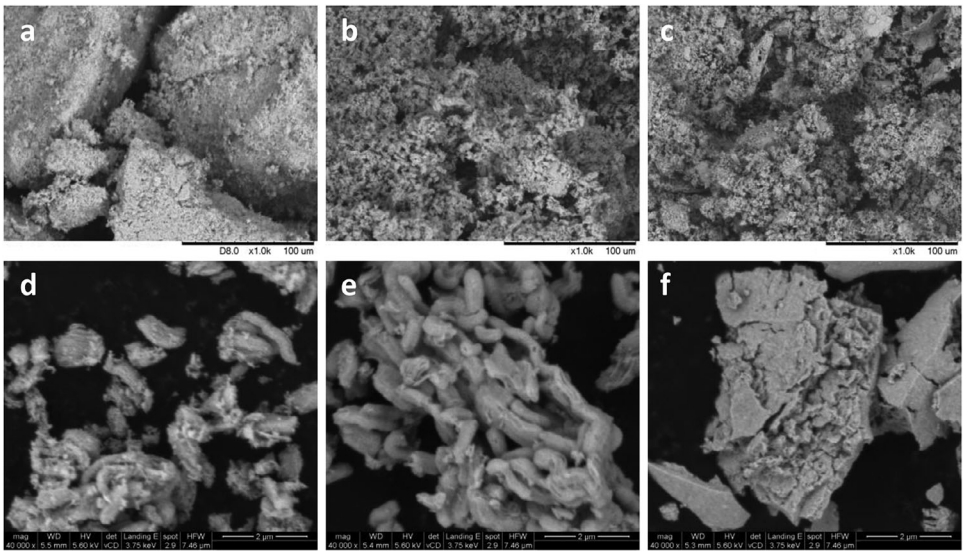

Figure 3. SEM images at different magnifications for a,d) NiCe-imp, b,e) NiCe-mix, and c,f) NiCe-sg samples.

Table 2. Elemental analysis and textural properties of the samples.

Sample	Composition (at %)			S_{BET}	Pore Volume
	Ni/Ce[a]	Ni/M[b]	La/M[b]	(m^2 g^{-1})	(cm^3 g^{-1})
SBA-15				775	0.98
NiCe-imp	11.0	12.7		125	0.38
NiCeLa-imp		12.7	7.8	141	0.39
NiCe-mix	11.5	11.0		143	0.35
NiCeLa-mix		12.2	8.0	161	0.34
NiCe-sg	9.5	10.1		3	0.02
NiCeLa-sg		10.3	7.9	6	0.03

[a] Derived. from SEM-EDX.
[b] m X-ray fluorescence. M=Ni + Ce or M=Ni + Ce + La.

smaller Ni cation keeping the octahedral coordination, creating weakly or under-coordinated oxygen atoms that are more easily removed in reactions involving the partial reduction of CeO_2.[27]

3.2. Microscopy Study

Figure 3 shows SEM images at different magnification for some of the Ni catalysts. For the mesoporous catalysts prepared by the hard template method, NiCe-imp and NiCe-mix samples, the typical rod-like morphology resembling that of the SBA-15 template can be seen (Figures 3d,e). The size of the short rods was relative uniform, with a mean size in the range 0.8–1.2 µm. However, sample prepared by impregnation exhibited a higher proportion of aggregates of nanoparticles of smaller size indicating that the original structure of the template was not completely maintained. On the other hand, the catalyst prepared by sol-gel showed the aggregation of particles resulting in porosity in the macroporous range. The EDX analysis showed that the Ni/Ce-ratios (Table 2) agree very well with the nominal values, indicating the succeed preparation of the catalysts. The bulk compositions were also corroborated by XRF analysis.

The morphology of the samples has been also examined by TEM. First, the TEM images for the SBA-15 used as template confirm the 2D hexagonal structure (p6mm plane group), with the typical morphology of curved cylinders (Figure 4) that exhibit a well-ordered hexagonal array of uniform mesopore channels when the electron beam is parallel to the main axis (see zone marked with arrow in Figure 4b). The pore channel diameter can be roughly estimated to about 6 nm.

Figure 5 shows the TEM images obtained for the as-prepared NiCeLa-mix and NiCeLa-sg samples. The NiCeLa-mix catalyst mainly consists of large arrays of uniform nanorods having a certain ordered framework, illustrating that this material is a negative replica of the mesoporous silica structure matrix. The diameter of the rods is about 5–8 nm consequence of the confined growth in the channels of the SBA-15 template. In addition, the mesoporous structure, i.e., the space between the rods, shows corrugated channels. Besides, some aggregates of particles are also seen, with sizes in the same range than the rods, ranges from 3 to 6 nm, which is in good agreement with XRD values (see Table 1). These results seem to suggest a limited or insufficient pore channel filling with the precursors that may be due to weak interactions between the metal precursors and the parent silica surface. Other possibility is the rupture of the original template structure due to pressure effects derived from the decomposition of the precursors during calcination. However, the fact that the main structure is maintained would indicate than the rods are connected by spacers. Then, during the synthesis, the metal precursors seem to have filled the random channel-interconnecting micropores within the SBA-15 walls that interconnect the main channels. Similar structures have been observed for mesoporous materials obtained using SBA-15 as template.[18,25,28,29] Well-defined lattice planes can be observed in several nanocrystallites in Figure 5c, with spacings of 0.31 nm and 0.27 nm that are assigned to (111) and (200) planes of CeO_2 (JCPDS PDF # 43–1002) indicating the existence of cubic crystalline ceria.

On the other hand, the aggregates of particles shown in the TEM images for NiCeLa-sg (Figure 5d,e), clearly reflect the high crystallinity of the sample and that the particles size is higher than for the other materials as the XRD also suggested.

Since the identification of nickel and lanthanum could not be clearly done by TEM, the distribution of the elements in the catalysts was studied on different regions of the catalysts by annular dark-field scanning transmission electron microscopy (ADF-STEM) investigations and the corresponding energy dispersive X-ray spectroscopy (EDS) microanalysis. Representative regions can be found in Figure 6 for NiCeLa-imp and NiCeLa-mix samples. For NiCeLa-imp sample, it is possible to note that while lanthanum is well dispersed, nickel seems to be well dispersed in some areas and concentrated in others, which indicate an aggregation of Ni particles (average sizes around 30–50 nm). Contrarily, for NiCeLa-mix, cerium, lanthanum and nickel are highly and uniformly dispersed over the entire area and no segregated domains of individual oxide phases of Ni or La are present within the sample. In addition, EDS analyses show that most of the silica template has been removed, although not completely. On the other hand, NiCeLa-sg shows (Figure 7) a behavior more similar to that NiCeLa-imp, with lanthanum well dispersed and areas where Ni is concentrated.

3.3. N_2 Adsorption-Desorption Isotherms

The N_2 adsorption-desorption isotherm and the corresponding pore size distribution of the SBA-15 used as a template are presented in Figure 8. It can be seen that the isotherm is type IV with a hysteresis loop H1 attributed to uniform, cylindrical mesopores of channels in a narrow size range. The BET specific area and pore volume are between 775 $m^2 \cdot g^{-1}$ and 0.9 $cm^3 \cdot g^{-1}$, respectively and the pore distribution indicates an average pore diameter of 5.7 nm.

The supports and catalysts replicas synthesized using SBA-15 as a template also show the typical IV shape adsorption isotherms, Figure 8, although in this case the hysteresis loops are less well-defined and would be classified as type H3. Therefore, pore shapes and widths are less uniform, probably slit-like. This

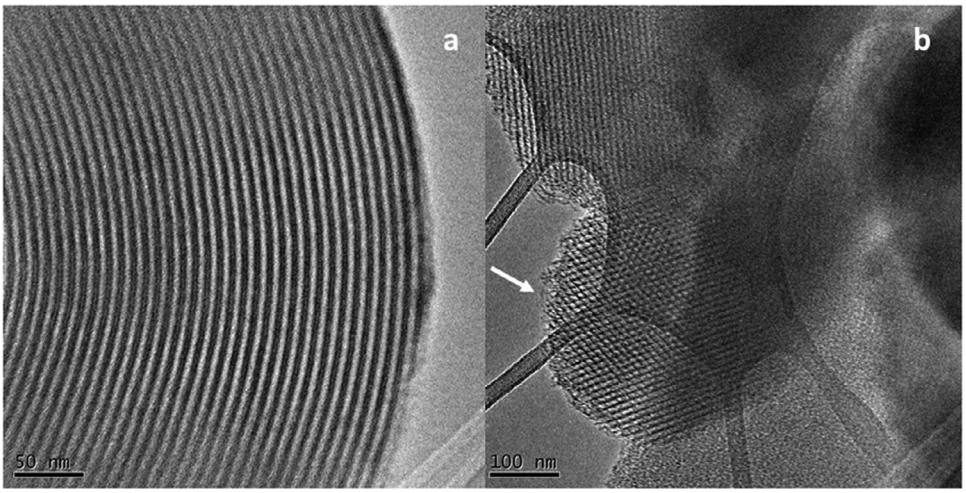

Figure 4. TEM images of the SBA-15 used as template.

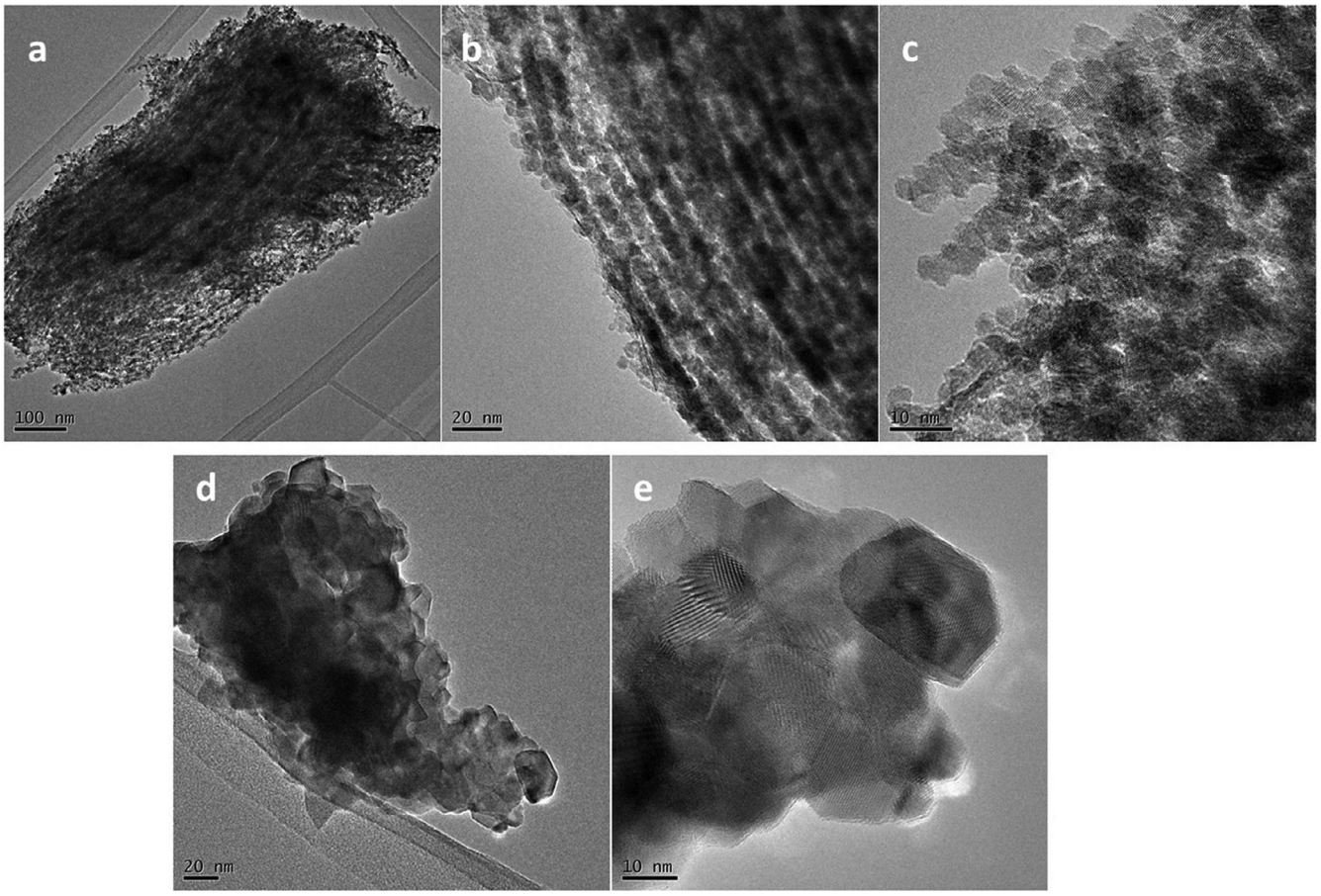

Figure 5. TEM images of nanoparticle arrays for as-prepared a–c) NiCeLa-mix replica of SBA-15 silica template and d,e) NiCeLa-sg catalyst.

confirms the pore shape that is to be expected for mesoporous replica structures obtained from SBA-15 silica.[20,26]

On the other hand, the isotherms for NiCe-sg and NiCeLa-sg have characteristics of type II and IV, which are assigned to materials with both mesopores and macropores.[23] The isotherm of NiCe-sg shows a minimal hysteresis loop in the larger pores range at relative pressures of 0.9–1.0; the adsorption and desorption curves are nearly vertical, suggesting the presence of significant mesopores with a variety of pore sizes extending into the macropore range. In contrast, the NiCeLa-sg sample, exhibits a broader hysteresis loop at relative pressures of 0.6–0.9, pointing to a higher proportion of smaller mesopores compared with NiCe-g. In both cases, the presence of a significant external surface is confirmed by the isotherms.

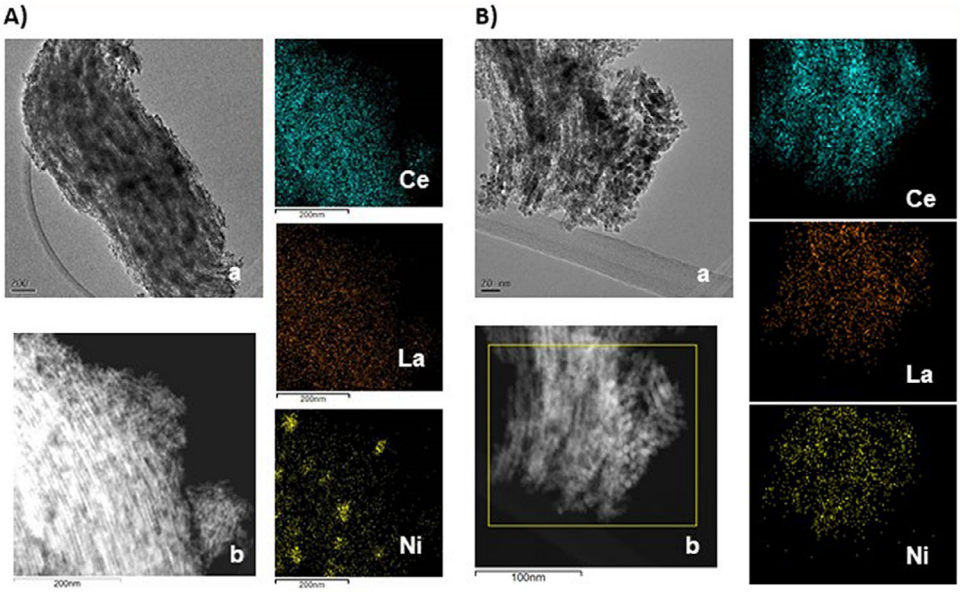

Figure 6. a) Representative TEM micrograph and b) dark-field STEM image with corresponding EDS elemental maps of the selected area showing the chemical distribution of Ce (cyan), La (orange) and Ni (yellow) of A) NiCeLa-imp and B) NiCeLa-mix catalysts.

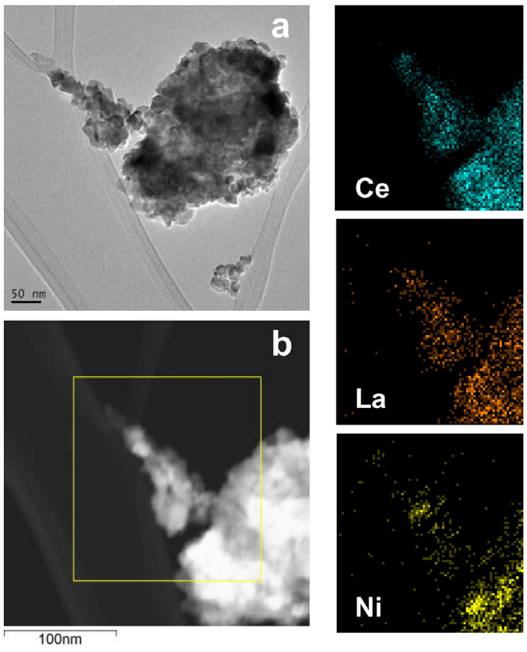

Figure 7. a) Representative TEM micrograph and b) dark-field STEM image with corresponding EDS elemental maps of the selected area showing the chemical distribution of Ce (cyan), La (orange) and Ni (yellow) of NiCeLa-sg catalyst.

The specific areas obtained by applying the BET equation, average pore sizes and pore volumes are shown in Table 2. Surface areas for mesoporous materials varied in the range 125–161 $m^2 \cdot g^{-1}$. The average pore diameters obtained from the desorption branch and applying the BJH method are between 8 and 15 nm. The pore size distribution curves suggest a possible bimodal mesoporous structures with sizes around 3 and in the range 13–20 nm. The differences in the type of pore and its size are due to the fact that, during calcination, being above the decomposition temperature of the precursor, it decomposes and oxidizes, forming cerium oxide within the pores of the SBA-15. On the other hand, the samples prepared by sol-gel have very low surface areas of 3 and 6 $m^2 \cdot g^{-1}$ for NiCe-sg and NiCeLa-sg, and a low degree of porosity.

3.4. Temperature Programmed Reduction

The temperature-programmed hydrogen reduction (H_2-TPR) profiles for NiCe-imp, NiCeLa-imp, NiCe-mix, NiCeLa-mix, NiCe-sg, and NiCeLa-sg are shown in Figure 9, clearly revealing that preparation methods have a great influence in the reducibility of the samples. For the mesoporous samples, several hydrogen consumption peaks are observed in the range 423–823 K, which points to the existence of different Ni species. In general, for NiO-CeO_2 systems, up to five hydrogen consumption peaks could be present: α_1 and α_2 peaks corresponding to reductions of surface adsorbed oxygen species (in oxygen vacancies) and interfacial oxygens in Ni-O-Ce sites, β peak derived from bulk NiO reduction with moderate interaction with CeO_2, γ peak of highly dispersed NiO with strong interactions with ceria and, at the highest temperature, the δ peak corresponding to bulk ceria reduction.[30–32]

NiCe-imp sample showed a profile characteristic of a conventional Ni (II) oxide supported catalyst with a main H_2 consumption peak with maximum at 673 K (β peak), a shoulder around 715 K (γ peak), derived from reduction of bulk NiO in two steps $NiO \rightarrow Ni^{\delta+} \rightarrow Ni^0$, and a small and wide α peak around 573 K. The wide peak at temperatures higher that 973 K can be assigned to ceria reduction (δ peak). On the other hand, NiCeLa-imp sample displayed a more complex profile where the surface adsorbed oxygen reduction starts a lower temperature (473 K) and its contribution has increased. The formation of these

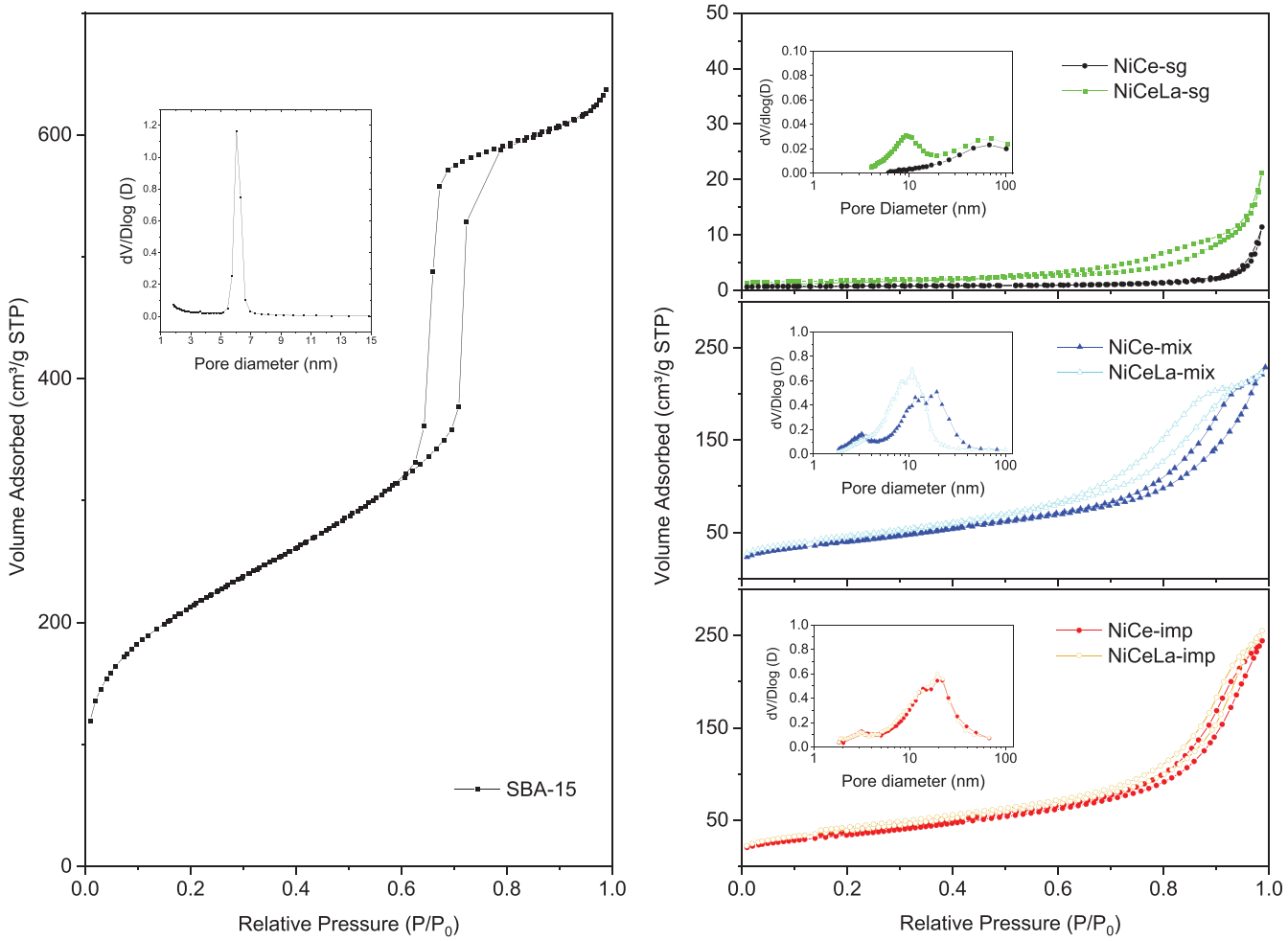

Figure 8. N_2 adsorption-desorption isotherms for the SBA-15 used as template (left) and catalysts (right).

active oxygen species, easily reducible by H_2 at low temperature is consequence of the generation of oxygen vacancies due to the incorporation of La^{3+} ions into the ceria lattice as the XRD has illustrated. Furthermore, the peak derived from reduction of surface ceria is slightly shifted to lower temperature, around 953 K, which is also consequence of the doping with La that favors oxygen lability and mobility in a larger volume cell during the reduction process.[23]

For samples NiCe-mix and NiCeLa-mix, it is clear the occurrence of signals at the temperatures in the range between 473 and 623 K corresponding to α_1 and α_2 peaks, i.e., reduction of surface-adsorbed oxygen species. In this case, the formation of active oxygen species even in the sample without La, can be due to the charge unbalance and lattice distortion occurring within the structure of CeO_2 after replacement of some Ce^{4+} by the incorporated Ni^{2+} that has a smaller radius. The peak observed at around 660 K (β peak) can be attributed to the reduction of NiO crystallites highly dispersed and interacting with the support or to the reduction of Ni-O-Ce sites. This would be confirmed, as described above, by the EDX-mapping and the absence of reflections due to NiO in the XRD analysis.

Compared to NiCe-mix and NiCeLa-mix, in the reduction of NiCe-sg and NiCeLa-sg, the maximum of the main peak is shifted to lower temperatures, 604 and 623 K, respectively, pointing to more easily reducible Ni species. In addition, the main peaks showed a shoulder at the higher temperature side, 635 and 653 K respectively, reflecting again the reduction of Ni species in two steps. The H_2 consumption of γ peak is lesser than that of β peak, suggesting that NiO can be reduced to a great degree during the first step. The slightly higher temperatures observed for NiCeLa-sg sample can be explained by the doping with La that increases the metal-support interaction.[23,33] Incorporation of La also modified the reduction of the ceria support as it was shown for the rest of the doped samples, and the peak is shifted from 1073 K, for NiCe-sg, to 973 K for NiCeLa-sg. Only for NiCe-sg sample a very small peak at 522 K would indicate the presence of a low amount of surface oxygen species. Then, these results of H_2-TPR illustrate that in NiCe-sg and NiCeLa-sg catalysts, most Ni species existed in the form of NiO particles dispersed on the support.[23]

3.5. XPS Analysis

Figure 10 displays the Ce *3d* and O *1s* core levels XP spectra for Ni samples after reduction at 873 K for 2 h. The spectra for the

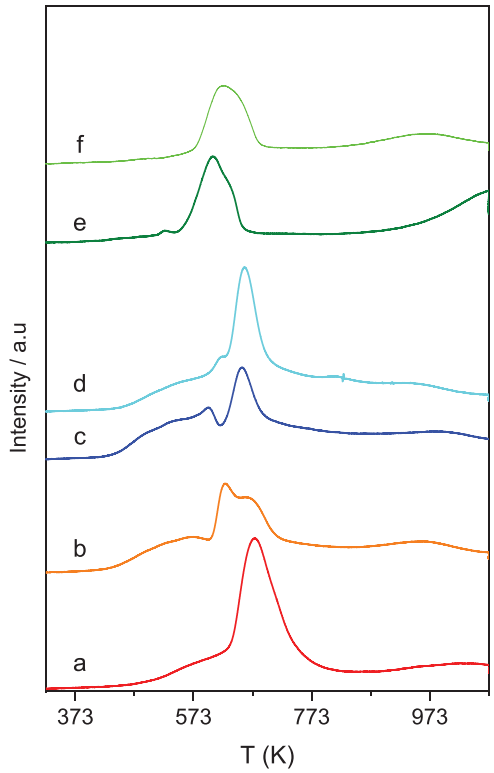

Figure 9. H_2-TPR profiles for the prepared catalysts: a) NiCe-imp, b) NiCeLa-imp, c) NiCe-mix, d) NiCeLa-mix, e) NiCe-sg, and f) NiCeLa-sg.

nonreduced NiCe-imp (NiCe-imp-fresh) sample have been also included for comparison. The rest of the spectra for the nonreduced samples are displayed in Figure S2. Following peak fitting models and as reported previously,[34,35] the Ce *3d* region was deconvoluted into 10 peaks. Both Ce^{4+} and Ce^{3+} species were present in the catalyst surface, as the characteristic multiplets of $3d_{5/2}$ and $3d_{3/2}$ core holes were observed. Peaks at 882.02, 887.79, 897.51, 899.59, 906.78, and 916.6 eV are attributed to Ce^{4+} species (*v*, *v″*, *v‴*, *u*, *u″*, and *u‴*) and peaks at 882.02, 887.79, 897.51, 899.59 eV are assigned to Ce^{3+} (v_0, v', u_0, and u'). Assignments are defined in Figure 10A for NiCe-imp-fresh sample as reference. The calculated values for surface relative amount of Ce^{3+}, considering the relative area of u_0, v_0, u', *and* v' peaks to the area of the Ce 3d region are reported in Table 3 for all the catalysts, fresh and after reduction. Initially, all samples show proportions of Ce^{3+} in the range 14%–23% that are common for ceria nanoparticles.[36] After the reduction treatment, it is observed an increase in the proportion of Ce^{3+} for all the samples. Notably, mesoporous Ni samples, regardless of the method of incorporation of Ni, showed a higher proportion of Ce^{3+} than those prepared by the sol-gel method.

The XPS spectra of O *1s* core level for samples after reduction at 873 K for 2 h are shown in Figure 10B. A spectrum for the non-reduced NiCe-imp sample has been included for comparison. The rest of the spectra for the nonreduced samples are displayed in Figure S3. For the nonreduced samples, three components were observed: a main peak around 529.0 eV, assigned to surface lattice oxygen (O_{Latt}); a peak at 531.3 eV attributed to surface adsorbed oxygen ions on surface oxygen vacancies (O_{ads}); and a peak at higher energy, 533.5 eV, assigned to molecular water or OH surface groups.[37] It is seen that the proportion of the peak assigned to O_{ads} related to the vacancies of oxygen follows a tendency, i.e., higher proportion for mesoporous catalysts, which is consistent with the TPR profiles

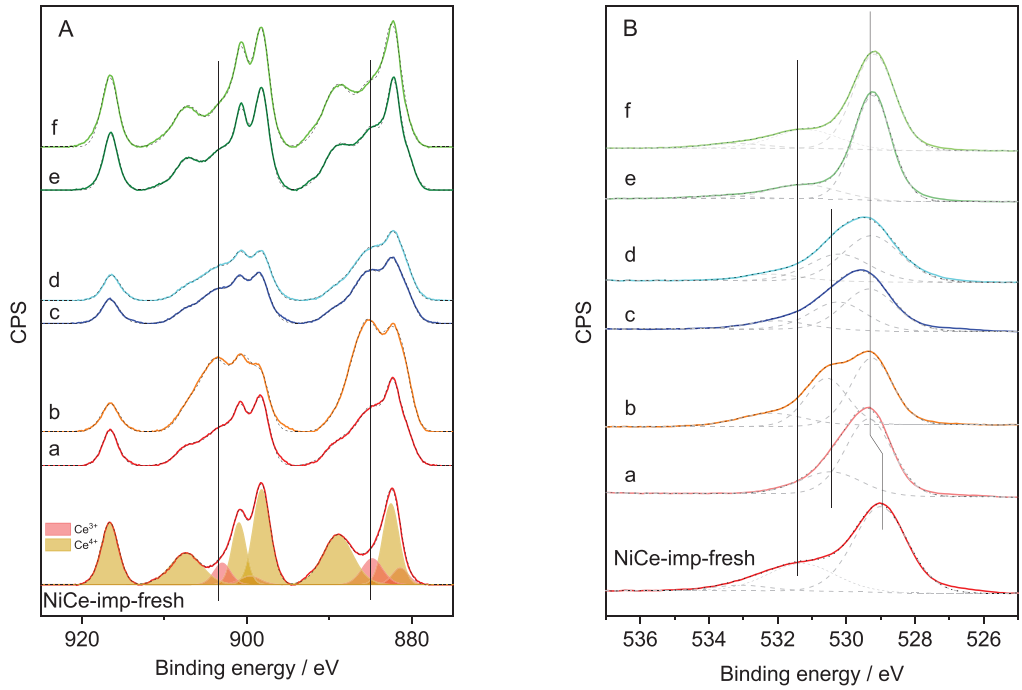

Figure 10. A) Ce *3d* and B) O *1s* core levels XP spectra for samples a) NiCe-imp, b) NiCeLa-imp, c) NiCe-mix, d) NiCeLa-mix, e) NiCe-sg, and f) NiCeLa-sg samples after reduction at 873 K. Spectra for the non-reduced NiCe-imp sample are shown as reference.

where α peaks (associated to adsorbed oxygen species) were more intense for the mesoporous materials. After reduction of the samples, different behaviours were observed depending on the sample. For samples prepared by the sol-gel method, only a slight decrease in the peak at 531.3 eV was detected after reduction. However, for the mesoporous samples, the main peak was shifted to higher BE, 529.4 eV. In addition, the asymmetry of the peak seems to suggest a contribution from another component at the high energy side, 530.5 eV, more prominent on the NiCeLa-imp sample. This latter peak can be assigned to oxygen atoms bound to Ce^{3+} species. It has been reported that the O *1s* photoemission peaks for oxygen bound to Ce^{4+} or Ce^{3+} exhibited different binding energies. So, binding energy shifts from 0.3 eV up to 1–2 eV for the O 1s photoemission peak have been reported previously when the transformation from CeO_2 to Ce_2O_3 occurs.[38–40] Besides, the shift observed in Figure 10B for -imp and -mix samples after reduction would be in line with the increase in the calculated proportion of Ce^{3+} after reduction treatment.

Figure 11A,B depict the Ni $2p_{3/2}$ core level spectra of fresh and reduced catalysts without the La dopant, respectively. Samples doped with La could not be analysed since the La 3d transition overlaps in this energy region. This spectral region shows a main band in the range 851–859 eV together with a satellite structure at higher BE (859–866 eV).[41] Regarding fresh catalysts, three peaks were observed in the main region centred at around 853.2, 855.0, and 857.2 eV, which can be assigned to surface NiO species, Ni^{2+} species in interaction with ceria support (Ni-O-Ce species) and Ni cations with high positive charge density as $Ni(OH)_2$ species, respectively.[42] In addition, the mesoporous catalyst prepared by impregnation (NiCe-imp) presented a small shoulder at lower BE, 852.3 eV, that could be assigned to Ni^0 species and therefore, reflects the partial reduction of Ni, due to the vacuum and incident X-ray during the XPS analyses. The proportion of surface NiO and Ni in interaction with ceria varies depending on the method of preparation. The catalyst prepared by impregnation (NiCe-imp) presents the highest proportion of surface NiO and, therefore, the least amount of Ni in intimate contact with the support. This percentage of surface NiO decreases if Ni is incorporated during the preparation of the materials, samples NiCe-sg and NiCe-mix, at the expense of an increase of the Ni^{2+} species in intimate contact with the support (Ni-O-Ce), being the catalyst prepared by mixing (NiCe-mix) the one that presents the greatest contact between ceria and Ni phases.

For the reduced catalysts, the main peak developing at 852.5 eV was assigned to metallic Ni. The reduction seems more severe NiCe-imp sample than for the other two samples where contributions at higher binding energies were still observed, revealing the presence of Ni in higher oxidation states. It is remarkable the high proportion of NiO species on NiCe-sg sample. It is also interesting that while for NiCe-imp sample the Ni/Ce ratio (Table 3) increased after reduction, it decreased for NiCe-mix and NiCe-sg. This is probably due to a segregation of the Ni to the surface after the reduction treatment for the impregnated sample and to the metal-support effect for NiCe-mix and NiCe-sg.[43]

3.6. RWGS Reaction

Figure 12 shows the CO_2 conversion, CO selectivity and CO yield values for the synthesized catalysts. It can be seen that the mesoporous catalysts have initial conversions of 46%–47%, close to the equilibrium conversion in the rWGS reaction calculated for a ratio $H_2/CO = 2$ and temperature of 873 K, which is 51.6%. For

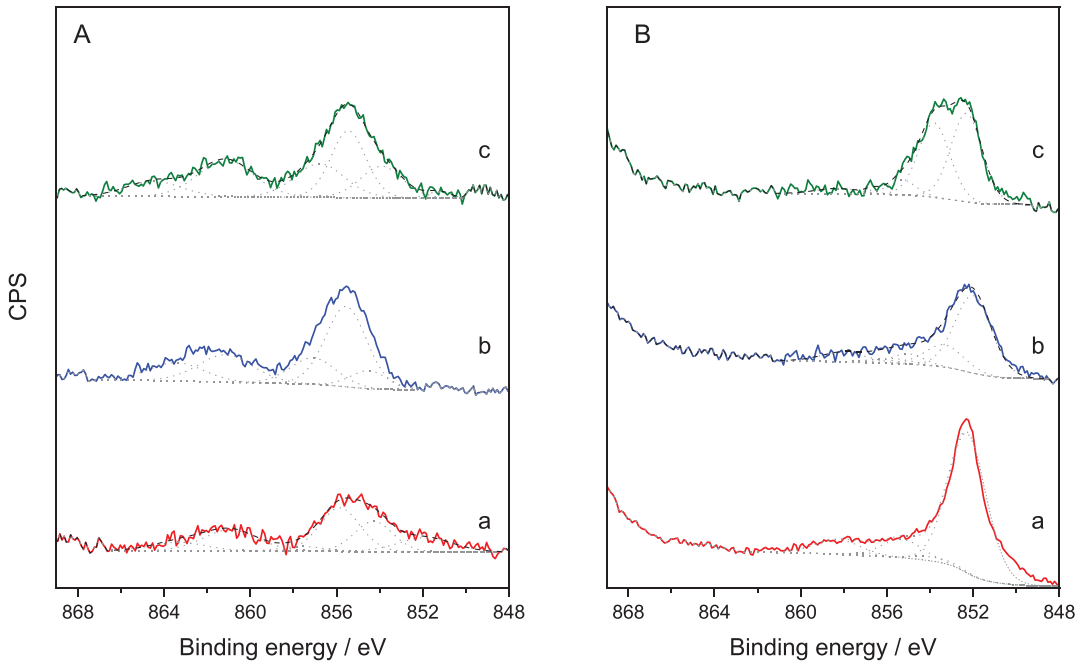

Figure 11. Ni $2p_{3/2}$ core levels XP spectra for A) fresh samples and B) after reduction at 873 K. a) NiCe-imp, b) NiCe-mix, and c) NiCe-sg.

Table 3. XPS results for the fresh and reduced catalysts: surface Ce^{3+} concentration and surface Ni/Ce atomic ratio.[a)]

Catalyst	$Ce^{3+}/(Ce_{total})$ (%)	Ni/Ce
NiCe-imp	13.7(42.2)	0.062(0.182)
NiCeLa-imp	20.5(65.5)	
NiCe-mix	20.1(51.4)	0.158(0.080)
NiCeLa-mix	20.7(52.9)	
NiCe-sg	22.9(32.2)	0.104(0.044)
NiCeLa-sg	16.3(25.4)	

[a)] Values in parenthesis for reduced samples

these catalysts, doping with La slightly increases the conversion values. Furthermore, within these mesoporous catalysts, those prepared by impregnation on the mesoporous supports, NiCe-imp and NiCeLa-imp show greater deactivation with time in reaction. On the other hand, the catalysts prepared by the sol-gel method give significantly lower conversion values. This phenomenon could be attributed to its smaller specific area, with a smaller number of active sites exposed per catalyst weight, as the Ni/Ce XPS ratios in Table 3 have shown. In addition, these sol-gel catalysts presented the lowest proportion of Ce^{3+}, which is related with a lesser surface interface metal-support, since metal phase promotes ceria reduction.[44]

In order to understand the different performance of the catalysts, the structure of the catalysts after the RWGS reaction was analysed by TEM-STEM. Representative images obtained for NiCeLa-imp and NiCeLa-mix are presented in Figure 13. As indicated previously, the catalysts mainly consist of large domains having a certain ordered framework and uniform nanoparticles, which were maintained after the reaction.

Additional elemental mapping analyses from the corresponding STEM-EDS data for NiCeLa-imp and NiCeLa-mix (Figure 14) after reaction, still confirms the homogeneous distribution of La on the ceria, implying that it is well dispersed on the samples or embedded in the lattice of ceria. As far as Ni is concerned, differences are clear. Some isolated domains or patches of nickel phases are evident for NiCeLa-imp sample as occurred on the fresh sample. However, they seemed bigger which could explain the lower conversion values and higher deactivation with time in reaction. For the sample NiCeLa-mix some aggregation of Ni after reaction is also observed but in a much lower extent, which agrees with the lower degree of deactivation in reaction. This pointed again to Ni interacting more strongly with the support and to the existence of Ni—O—Ce species that can limit the agglomeration of the particles.

Therefore, the reason for the higher stability of the "-mix" catalysts is the mesoporous structure with channels formed by stacked particles that seems to facilitate the dispersion of the Ni particles after reduction which results in the exposure of more Ni active sites and to prevent carbon deposits formation and the consequent deactivation of the active sites. On the other hand, the much greater porosity of these samples favours heat release, decreasing the formation of hot spots.

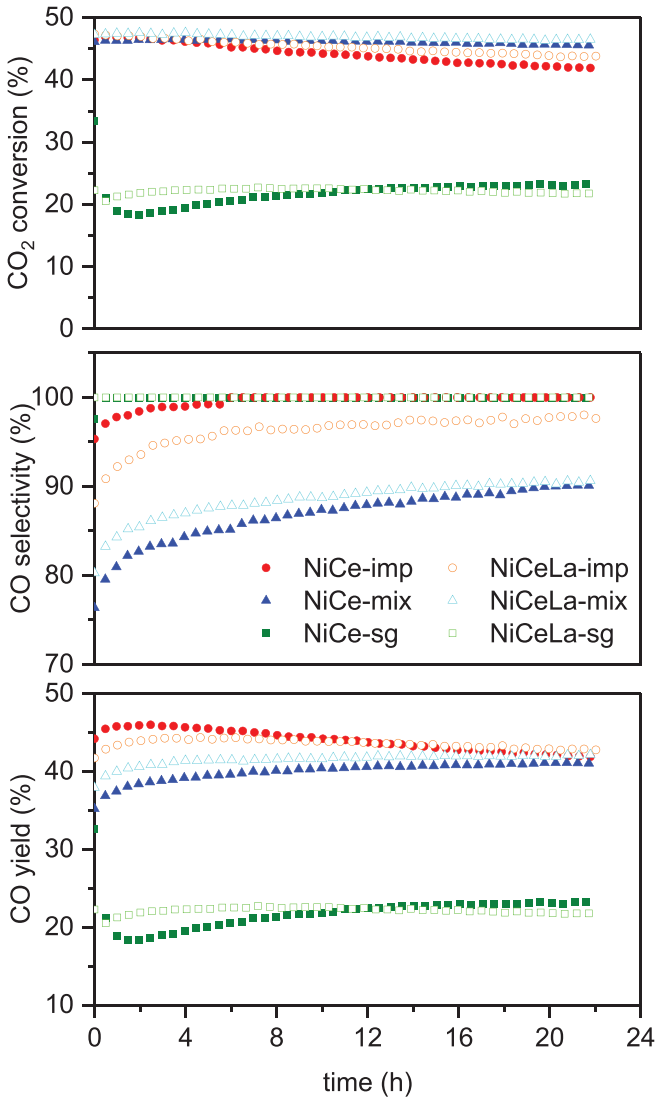

Figure 12. Catalytic performance of the prepared samples (CO_2 conversion, CO selectivity and CO yield) versus reaction time. (Reaction conditions: 873 K, $H_2/CO_2 = 2$, molar, 600,000 $mL_N \cdot h^{-1} \cdot g^{-1}$).

Concerning the selectivity to CO, it seems to be inversely related to conversion. Thus, the catalysts prepared by sol-gel gave a CO selectivity of 100%. Meanwhile, mesoporous catalysts provided lower selectivities, detecting CH_4 as a by-product, and following the global order of CO selectivity of: "-mix" catalysts < "-imp" catalysts. Furthermore, for the mesoporous samples, it is observed an induction period where selectivity increases with time. As previously reported, this increase in CO selectivity with time in reaction is related to the progressive reduction of surface Ni species to metallic nickel during the reaction.[23] For the NiCe-imp sample this induction period takes 6 hours, being achieved 100% of CO selectivity; for the NiCeLa-imp sample, this period is ~20 h being reached around 97% of selectivity to CO. This different induction period is in accordance with the greater interaction of Ni species with the support containing lanthanum (NiCeLa-imp), as previously observed in the reduction profiles (Figure 9). In the case of the "-mix" samples, it is noteworthy that this period takes longer, around 18 and 21 h for

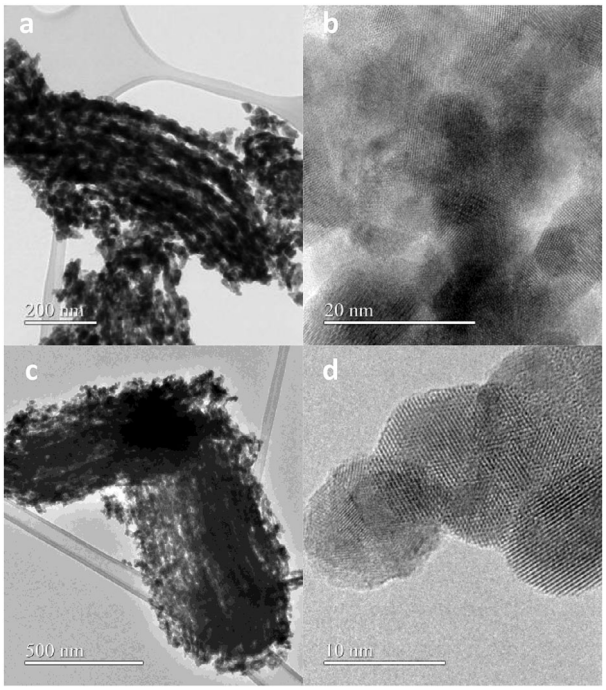

Figure 13. TEM images of nanoparticle arrays and HRTEM micrographs of the crystalline framework for a,b) NiCeLa-imp and c,d) NiCeLa-mix samples after reaction.

NiCeLa-mix and NiCe-mix respectively, being achieved ~ 90% CO selectivity after 22 h of reaction, being methane, the only other product detected. This lower CO selectivity value obtained with the "-mix" samples is explained by the greater surface proportion of Ce-V_{oxc}-Ni species, that favour methanation, when surface metallic nickel is also available.[41,45] So, CO_2 methanation is favoured when Ni is supported on a reducible metal oxide that is capable of developing the basicity associated with medium-strength basic sites and also with a suitable balance between metallic sites and metal sites linked to the support.[46,47] The lower methane production and faster induction period for the NiCe-imp and NiCeLa-imp catalysts is due to the minor extent of Ni-support interaction, since the NiO particles incorporated by impregnation on the mesoporous support are larger, as reflected by the XRD and the STEM-EDX mapping images for the La-doped sample.

Comparing the "-mix" samples with those prepared by sol-gel, where in both cases Ni was incorporated in situ during the preparation of the samples, the results of H_2-TPR (Figure 9) and XPS (Figure 10) demonstrated that smaller Ni particles and CeO_2 with more oxygen vacancies were obtained on "-mix" samples. On the other hand, despite the fact that reduction of Ni is achieved at lower temperatures on the sol-gel samples (see H_2-TPR), XPS has shown a higher proportion of NiO species dispersed on the surface. While, for "-mix" samples, part of the nickel was incorporated into the CeO_2 lattice as ions to form a solid solution, and other part existed in the form of NiO highly dispersed. It can be inferred that the proper balance between Ni^0 active sites for H_2-dissociation, and Ni—O—Ce interface sites for CO_2 chemisorption and further dissociation appears to have not been reached for these samples. However, the stability in conversion values and the increase of CO selectivity with time for the "-mix" samples indicate that the catalytic surface is evolving towards the proper balance of species.

Ultimately, this work confirms the potential of our Ni-mesoporous catalysts that present high stability and excellent catalytic performance as compared to other high-performing catalysts reported in literature when considering conversion, selectivity and yield (Table S1).

4. Conclusions

In this work, mesoporous catalysts based on Ni as the metal phase and CeO_2 or $Ce_{0.9}La_{0.1}O_x$ as oxides have been prepared by nanocasting, using two different approaches: (i) incorporating Ni by impregnation on the mesoporous support, NiCe-imp

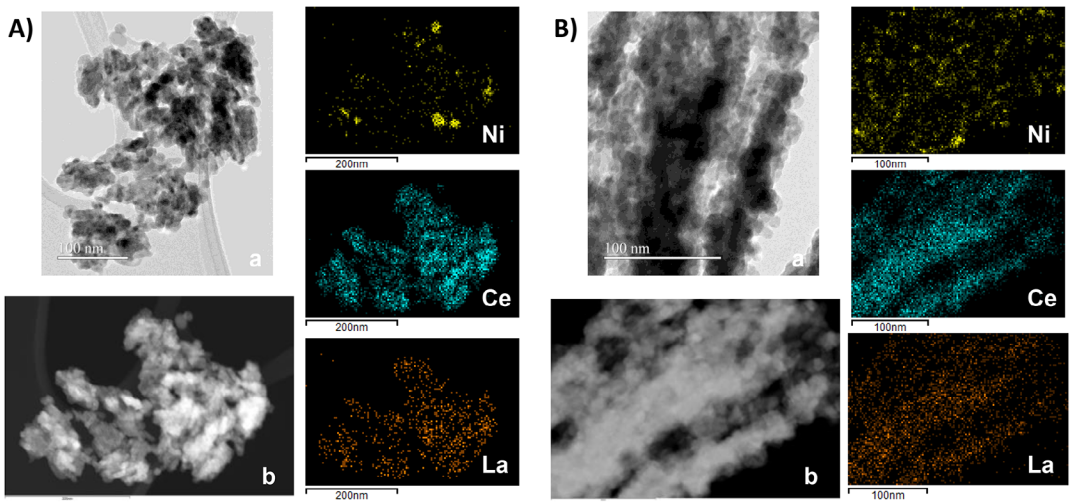

Figure 14. a) TEM image and b) corresponding high-angle annular dark field (HAADF) image and elemental mappings using energy dispersive X-ray spectroscopy (EDS) for A) NiCeLa-imp and B) NiCeLa-mix after RWGS.

and NiCeLa-imp, or (ii) through a "one-pot" strategy, introducing all the cations at the same time (NiCe-mix and NiCeLa-mix). The obtained materials have been characterized by different techniques and their catalytic performance has been studied in the RWGS and compared to samples with similar compositions prepared by sol-gel.

We have verified that the catalyst preparation method has a significant effect on the catalytic behavior and on the physicochemical properties of catalysts based on Ni-CeO_2 (with and without La as ceria dopant) as demonstrated by the results of XRD, TEM and STEM-EDX, N_2 adsorption-desorption isotherms, H_2-TPR, and XPS.

Mesoporous catalysts, prepared by hard-templating, both those prepared by incorporating Ni by impregnation, NiCe-imp and NiCeLa-imp, and the "one-pot" counterparts, NiCe-mix and NiCeLa-mix, have developed a mesoporous structure and a large specific surface area that increase the CO production by catalyst weight, compared to those prepared by sol-gel, since the larger porosity notably increases the dispersion of the active phases.

The lower CO selectivity observed in the "mix" catalysts prepared by one-pot hard-templating is related to the excessive metal-support interface that unbalance the ratio between metallic sites and oxygen vacancies linked to the support. This means that the largest metal-support interface does not mean, the greater selectivity to CO. Furthermore, NiCe-mix and NiCeLa-mix catalysts show great stability over time in reaction, which makes them promising candidates for this application.

Acknowledgments

We acknowledge grant PID2021-123287OB-I00 funded by MCIN/AEI/10.13039/501100011033 and by ERDF/UE. M.G.G. thanks the SECAT for a "Introducción a la Investigación en Catálisis" SECAT-Intro-2023 grant.

Conflict of Interests

The authors declare no conflict of interests.

Data Availability Statement

The data that support the findings of this study are available from the corresponding author upon reasonable request.

Keywords: Mesoporous ceria · Nanocasting · Ni · RWGS

[1] A. M. Bahmanpour, M. Signorile, O. Kröcher, *Appl. Catal. B: Environ.* **2021**, *295*, 120319.
[2] Y. A. Daza, J. N. Kuhn, *RSC Adv.* **2016**, *6*, 49675–49691.
[3] X. Chen, Y. Chen, C. Song, P. Ji, N. Wang, W. Wang, L. Cui, *Front. Chem.* **2020**, *8*, 709-729.
[4] X. Su, X. Yang, B. Zhao, Y. Huang, *J. Ener. Chem.* **2017**, *26*, 854–867.
[5] T. Mathew, S. Saju, S. N. Raveendran, in *Engineering Solutions for CO_2Conversion* (Eds: T. R. Reina, H. Arellano-Garcia, J. A. Odriozola), Wiley-VCH, Weinheim **2021**, pp. 281-316.
[6] S. S. Kim, H. H. Lee, S. C. Hong, *Appl. Catal., B* **2012**, *119*, 100–108.
[7] C. S. Chen, W. H. Cheng, S. S. Lin, *Appl. Catal., A* **2003**, *238*, 55–67.
[8] P. Ebrahimi, A. Kumar, M. Khraisheh, *Catalysts* **2022**, *12*, 1101.
[9] L. Yang, J. Gandara-Loe, L. Pastor-Pérez, Q. Zhang, Y. He, T. R. Reina, in *Chemical Valorisation of Carbon Dioxide* (Eds: G. Stefanidis, A. Stankiewicz), The Royal Society of Chemistry, Cambridge **2023**, pp. 208–228.
[10] C. Alvarez-Galvan, J. L. Martínez, M. Capel-Sanchez, L. Pascual, J. A. Alonso, *Adv. Sustain. Syst.* **2021**, *5*, 2100029-2100039.
[11] C. Alvarez-Galvan, P. G. Lustemberg, F. E. Oropeza, B. Bachiller-Baeza, M. Dapena Ospina, M. Herranz, J. Cebollada, L. Collado, J. M. Campos-Martin, V. A. de la Peña-O'Shea, J. A. Alonso, M. V. Ganduglia-Pirovano, *ACS Appl. Mater. Interfaces* **2022**, *14* 50739–50750.
[12] Y. Wang, H. Arandiyan, J. Scott, A. Bagheri, H. Dai, R. Amal, *J. Mater. Chem. A* **2017**, *5*, 8825-8846.
[13] Y. Cui, X. Lian, L. Xu, M. Chen, B. Yang, C. Wu, W. Li, B. Huang, X. Hu, *Materials* **2019**, *12*, 276.
[14] R. Kumar, B. Chowdhury, In *Advanced Functional Materials*, (Eds: A. Tiwari, and L. Uzun), Wiley, Hoboken, NJ **2015**.
[15] B. Szczęśniak, J. Choma, M. Jaroniec, *Mater. Adv.* **2021**, *2*, 2510–2523.
[16] M. Dubey, S. Wadhwa, A. Mathur, R. Kumar, *Appl. Surf. Sci. Adv.* **2022**, *12*, 100340.
[17] S. Chatterjee, K. Bhaduri, A. Modak, M. Selvaraj, R. Bal, B. Chowdhury, A. Bhaumik, *Mol. Catal.* **2021**, *502*, 111381–111388.
[18] E. Rossinyol, J. Arbiol, F. Peiró, A. Cornet, J. R. Morante, B. Tian, T. Bo, D. Zhao, *Sensors and Actuators B* **2005**, *109*, 57–63.
[19] S. C. Laha, R. Ryoo, *Chem. Commun.* **2003**, 2138–2139.
[20] L. Zhang, M. Jaroniec, *J. Colloid Interface Sci.* **2017**, *501*, 248–255.
[21] D. Zhao, Q. Huo, J. Feng, B. F. Chmelka, G. D. Stucky, *J. Am. Chem. Soc.* **1998**, *120*, 6024–6036.
[22] M. Choi, W. Heo, F. Kleitz, R. Ryoo, *Chem. Commun.* **2003**, 1340–1341.
[23] B. Bachiller-Baeza, J. E. F. S. Rodrigues, M. Capel-Sanchez, J. Gainza, V. E. García-Sánchez, I. J. Villar-García, V. Perez-Dieste, C. Marini, M. T. Fernández-Diaz, J. A. Alonso, C. Álvarez-Galván, *J. CO2 Util.* **2024**, *89*, 102969.
[24] N. Fairley, V. Fernandez, M. Richard-Plouet, C. Guillot-Deudon, J. Walton, E. Smith, D. Flahaut, M. Greiner, M. Biesinger, S. Tougaard, D. Morgan, J. Baltrusaitis, *Appl. Surf. Sci. Adv* **2021**, *5*, 100112.
[25] D. Zhao, J. Feng, Q. Huo, N. Melosh, G. H. Fredrickson, B. F. Chmelka, G. D. Stucky, *Science* **1998**, *279* 548–552.
[26] M. García Ruiz, J. Aguilar Pliego, L. E. Noreña Franco, C. Márquez Álvarez, J. Pérez Pariente, N. C. Martin Guaregua, *J. Appl. Res. Tech.* **2018**, *16*, 511-523.
[27] A. B. Kehoe, D. O. Scanlon, G. W. Watson, *Chem. Mater.* **2011**, *23*, 4464–4468.
[28] W. Yue, W. Zhou, *Chem. Mater.* **2007**, *19*, 2359–2363.
[29] S. Jun, S. H. Joo, R. Ryoo, M. Kruk, M. Jaroniec, Z. Liu, T. Ohsuna, O. Terasaki, *J. Am. Chem. Soc.* **2000**, *122*, 10712–10713.
[30] L. Pino, A. Vita, F. Cipitì, M. Laganà, V. Recupero, *Catal. Lett.* **2008**, *122*, 121–130.
[31] E. T. Saw, U. Oemar, X. R. Tan, Y. Du, A. Borgna, K. Hidajat, S. Kawi, *J. Catal.* **2014**, *314*, 32-46.
[32] Y. Li, B. Zhang, X. Tang, Y. Xu, W. Shen, *Catal. Commun.* **2006**, *7*, 380–386.
[33] J. G. Nunan, M. J. Cohn, J. T. Dormer, *Catal. Today* **1992**, *14*, 277–291.
[34] P. Burroughs, A. Hamnett, A. F. Orchard, G. Thornton, *J. Chem. Soc. Dalt. Trans.* **1976**, *17*, 1686.
[35] M. Roméo, K. Bak, J. El Fallah, J. F. Le Normand, L. Hilaire, *Surf. Interface Anal.* **1993**, *20*, 508–512.
[36] L. Cardenas, C. Molinet-Chinaglia, S. Loridant, *Phys. Chem. Chem. Phys.* **2022**, *24*, 22815-22822.
[37] J. A. Onrubia-Calvo, S. López-Rodríguez, I. J. Villar-García, V. Pérez-Dieste, A. Bueno-López, J. R. González-Velasco, *Appl. Catal. B: Environ.* **2024**, *342*, 123367.
[38] A. Pfau, K. D. Schierbaum, *Surf. Sci.* **1994**, *312*, 171.
[39] D. R. Mullins, S. H. Overbury, D. R. Huntley, *Surf. Sci.* **1998**, *409*, 307–319.
[40] J. P. Holgado, G. Munuera, J. P. Espinós, A. R. González-Elipe, *Appl. Surf. Sci.* **2000**, *158*, 164–171.
[41] A. P. Grosvenor, M. C. Biesinger, R. S.t.C. Smart, N. S. Mcintyre, *Surf. Sci.* **2006**, *600*, 1771–1779.
[42] A. Cárdenas-Arenas, A. Quindimil, A. Davó-Quiñonero, E. Bailón-García, D. Lozano-Castelló, U. De-La-Torre, B. Pereda-Ayo, J. A. González-Marcos,

J. R. González-Velasco, A. Bueno-López, *Appl. Mater. Today* **2020**, *19*, 100591.
[43] J. A. Farmer, C. T. Campbell, *Science* **2010**, *329*, 933-936.
[44] M. Xu, M. Peng, H. Tang, W. Zhou, B. Qiao, D. Ma, *J. Am. Chem. Soc.* **2024**, *146*, 2290–2307.
[45] S. Tada, H. Nagase, N. Fujiwara, R. Kikuchi, *Energy Fuels* **2021**, *35*, 5241–5251.
[46] V. V. González-Rangulan, I. Reyero, F. Bimbela, F. Romero-Sarria, M. Daturi, L. M. Gandía, *Catalysts* **2023**, *13*, 448.
[47] J. Tapia-Pérez, C. Ostos, C. Mendoza-Merlano, J. Arboleda-Echavarría, A. Echavarría-Isaza, *Environ. Technol. Innov.* **2024**, *35*, 103713.

Manuscript received: April 30, 2025
Revised manuscript received: July 9, 2025
Accepted manuscript online: July 16, 2025
Version of record online: ■■, ■■